

Lattice normal modes and electronic properties of the correlated metal LaNiO_3

Gaoyang Gou,^{1,*} Ilya Grinberg,^{1,†} Andrew M. Rappe,^{1,‡} and James M. Rondinelli^{2,3,§}

¹*The Makineni Theoretical Laboratories, Department of Chemistry,
University of Pennsylvania, Philadelphia, PA 19104, USA*

²*X-Ray Science Division, Argonne National Laboratory, Argonne, IL 60439, USA*

³*Department of Materials Science and Engineering,
Drexel University, Philadelphia, Pennsylvania 19104, USA*

(Dated: March 27, 2022)

We use density functional theory (DFT) calculations to study the lattice vibrations and electronic properties of the correlated metal LaNiO_3 . To characterize the rhombohedral to cubic structural phase transition of perovskite LaNiO_3 , we examine the evolution of the Raman-active phonon modes with temperature. We find that the A_{1g} Raman mode, whose frequency is sensitive to the electronic band structure, is a useful signature to characterize the octahedral rotations in rhombohedral LaNiO_3 . We also study the importance of electron–electron correlation effects on the atomic structure with two approaches which go beyond the conventional band theory (local spin density approximation): the local spin density+Hubbard U method (LSDA+ U) and hybrid exchange–correlation density functionals which include portions of exact Fock–exchange. We find the conventional LSDA accurately reproduces the delocalized nature of the valence states in LaNiO_3 and gives the best structural and vibrational agreement to the available experimental data. Based on our calculations, we show that the electronic screening effect from the delocalized Ni $3d$ and O $2p$ states mitigate the electronic correlations of the d^7 Ni cations, making LaNiO_3 a weakly correlated metal.

PACS numbers: 71.15.Dx, 63.20.dk, 78.30.Er, 79.60.Bm

I. INTRODUCTION

Conducting electrode materials are critical elements in the design of ultra-thin ferroelectric devices,^{1–4} magnetoresistive elements,⁵ and magnetoelectric multiferroic memories.⁶ The performance of perovskite-based heterostructures is intimately related to the electronic and atomic coherency across the electrode–oxide interface.⁷ For this reason, suitable metallic perovskite oxides that are structurally compatible with the active functional layers are highly desirable. LaNiO_3 (LNO) has found widespread use in this capacity,^{8–10} because it is a $3d$ transition metal oxide that shows no metal–insulator or spin state transitions.^{11,12} At present, it is also actively being pursued as the *functional* oxide component in devices that could harness an electric-field tunable Mott insulator transition (so called “Motttronic” applications),^{13–15} because it is the end-member of the rare-earth nickelate series—compounds with small charge-transfer gaps that are highly susceptible to temperature¹⁶ and pressure-induced^{17,18} electronic phase transitions.

Metallicity and magnetism in $3d$ transition metal (TM) oxides are strongly dependent on the valence bandwidth which originates from the hybridization between the TM $3d$ and O $2p$ orbitals.¹¹ In perovskite oxides like LNO, the hybridization derives from the structural connectivity of the NiO_6 octahedral units throughout the crystal. Small changes in the Ni–O–Ni bond angles and the Ni–O bond lengths, therefore, can dramatically alter the electronic properties. For example, tunable insulator–metal (IM) transition is obtained from the isovalent substitution¹⁹ of La: By increasing the rare-earth ionic radius such that the Ni–O–Ni bond angle approaches 180° , the charge-transfer

gap closes and the IM-transition becomes accessible above room temperature.

In addition to changes in the structural degrees of freedom, the small spatial extent of the $3d$ orbitals also reduce the valence bandwidth. This sufficiently enhances electron–electron correlation effects such that conventional band metals are often rendered insulating.²⁰ In LaNiO_3 , however, the strong Ni $3d$ – O $2p$ covalent interactions—formally it contains Ni^{3+} cations in a low-spin $3d^7$ configuration ($t_{2g}^6 e_g^1$)—are anticipated to reduce the correlation effects.²¹ Nonetheless, there are clear signatures indicative of important electron–electron interactions in the T^2 dependence of the resistivity and heat capacity measurements.^{11,22} Magnetic susceptibility data also reveal enhanced Pauli paramagnetism and effective carrier masses.^{16,23–26} Consistent with those studies, temperature dependent x-ray photoemission finds that the spectral weight of the Ni e_g band at the Fermi level increases upon cooling.²⁷ A fundamental question regarding the intrinsic properties of LaNiO_3 therefore still remains: which factors of the interwoven electronic and atomic structure support its metallic state?

In this work, we perform first-principles density-functional theory (DFT) calculations to investigate how hybridization between the Ni $3d$ and O $2p$ states and the structurally correlated NiO_6 octahedral framework respond to electron–electron interactions. We first examine the temperature-dependent rhombohedral to cubic structural phase transition using a Landau formalism²⁸ and *ab initio*-derived phenomenological coefficients obtained from the conventional band theory [local spin density approximation, (LSDA)]. In the rhombohedral phase, we compute the evolution of the Raman-active phonon modes

with temperature and find the LSDA results give excellent agreement with experiment. We then show how the A_{1g} Raman mode, which describes the rotation of adjacent NiO_6 octahedra, can be used as a structural indicator for the low-temperature rhombohedral phase.

To study the coupling between the lattice modes and the electronic structure, we compare conventional LSDA results with three other approaches designed to improve accuracy: the local spin density+Hubbard U (LSDA+ U) method, and two hybrid exchange-correlation functionals, PBE0^{29,30} and HSE,^{31,32} which contain mixtures of Fock-exchange added to the generalized gradient corrected DFT-functional of Perdew, Burke and Ernzerhof (PBE).³³ We then examine the electronic structure of LaNiO_3 by comparing the results obtained from the various functionals with the experimental photoemission spectroscopy (PES) and x-ray photoelectron spectroscopy (XPS) data. We find that the screening effects originating from the hybridized O $2p$ and Ni $3d$ electrons are sufficiently strong that they reduce the electronic correlations in LaNiO_3 .

II. CRYSTAL STRUCTURE AND RAMAN MODES

The crystallographic tolerance factor³⁴ for LaNiO_3 is $t=0.97$ and indicates that the aristotype cubic phase is susceptible to octahedral rotations because of an underbonded La–O coordination.²⁴ At ambient conditions, bulk LaNiO_3 crystallizes in a rhombohedral structure with space group $R\bar{3}c$ [Fig. 1(a)] and is related to the cubic perovskite through a trigonal lattice distortion along the $[111]$ -body diagonal.¹¹ It also exhibits octahedral rotations, which are equal in magnitude and alternate in “sense” about each Cartesian direction; this tilt system is classified according to Glazer notation^{35,36} as $a^-a^-a^-$ [Fig. 1 (b)]. Similar to other rhombohedrally distorted perovskites,³⁷ LaNiO_3 undergoes a temperature-induced

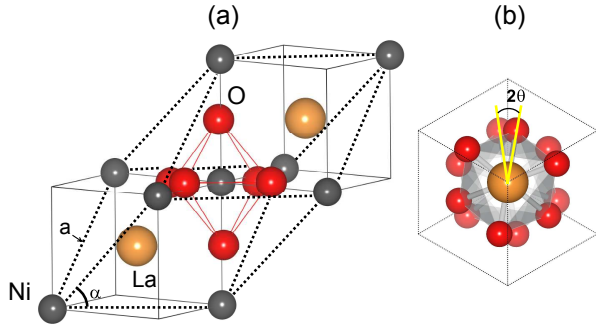


FIG. 1: (Color) (a) The crystal structure of rhombohedral $R\bar{3}c$ LaNiO_3 possesses anti-phase rotations ($a^-a^-a^-$ tilt system) of adjacent NiO_6 octahedra with angle θ (b) about the $[111]$ -trigonal axis. The relationship between the pseudo-cubic perovskite cell (solid lines) and the rhombohedral lattice vectors (dashed lines) of length a is also illustrated.

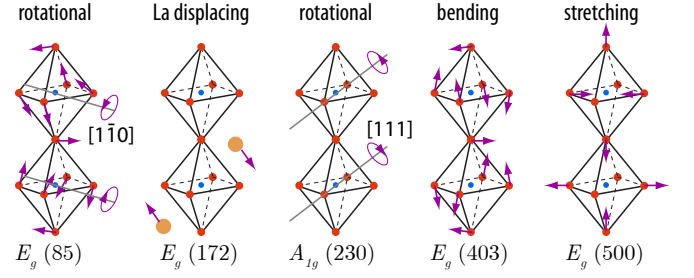


FIG. 2: (Color) Illustration of the displacement patterns for the Raman-active lattice normal modes in the $R\bar{3}c$ structure. The corresponding symmetry labels and our calculated LSDA frequencies (in cm^{-1}) are given for reference.

rhombohedral-to-cubic phase transition³⁸ upon heating: the NiO_6 octahedral rotation angle θ reduces continuously to zero in the cubic phase.

In the $R\bar{3}c$ space group, the La cations occupy the $2a(\frac{1}{4}, \frac{1}{4}, \frac{1}{4})$ Wyckoff positions while the Ni cations occupy the $2b(0, 0, 0)$ positions. The oxygen atoms are at the $6e(x, \bar{x} + \frac{1}{2}, \frac{1}{4})$ site, where x is the only free internal structural parameter that sets the rotation angle of the NiO_6 octahedra. These 10 atoms in the primitive rhombohedral unit cell give rise to 30 zone-center vibrational modes with the irreducible representations (irreps):

$$\Gamma = A_{1g} + 3A_{2g} + 4E_g + 2A_{1u} + 4A_{2u} + 6E_u.$$

where the E_g and E_u modes are two-dimensional irreps. The infrared-active and acoustic modes transform as the $4A_{2u} + 6E_u$, while the Raman active modes are given as $A_{1g} + 4E_g$. The A_{1g} and E_g Raman modes of the rhombohedral structure are mainly related to collective modes of the oxygen octahedral network (Figure 2): The A_{1g} mode describes the rotations of the NiO_6 about the trigonal $[111]$ -axis, and the E_g modes describe anti-parallel La displacements, Ni–O bond bending, stretching, and octahedral rotations about axes perpendicular to the $[111]$ -direction.

III. THEORETICAL METHODS

A. LSDA

We use two DFT implementations in this study, the QUANTUM ESPRESSO code (QE)³⁹ and the Vienna *ab initio* Simulation Package (VASP).^{40,41} Our reference electronic structure model to which we compare our advanced treatments of correlation effects is the frequently used local-spin density approximation (LSDA) exchange-correlation (XC) functional.⁴² Both codes flavors use the Perdew-Zunger parametrization⁴² of the Ceperley-Alder data⁴³ for the XC-functional. In all calculations, we constrain a collinear spin configuration for the Ni ions. The atomic positions in the rhombohedral structure are optimized by starting from the positions reported in Ref.11,

and the ionic coordinates are relaxed until the Hellmann-Feynman forces on the atoms are less than $0.1 \text{ meV } \text{\AA}^{-1}$.

VASP Details. We treat the core and valence electrons for all calculations in VASP using the projector augmented wave (PAW) method⁴⁴ with the following valence electron configurations: $5p^6 5d^1 6s^2$ (La), $3p^6 3d^9 4s^1$ (Ni), and $2s^2 2p^4$ (O) and a 650 eV plane wave cutoff. We use a Gaussian smearing of 0.05 eV over a $7 \times 7 \times 7$ Monkhorst-Pack k -point mesh⁴⁵ centered at Γ for the Brillouin zone (BZ) integrations (172 points are sampled in the irreducible BZ) in the 10-atom rhombohedral unit cell.

We obtain the phonon frequencies at the Γ -point by calculating total energies with respect to atomic displacements from the reference $R\bar{3}c$ structure. In this frozen-phonon method a series of small (symmetry inequivalent) atomic displacements are imposed along different Cartesian directions. We calculate the dynamical matrix from the Hellmann-Feynman forces⁴⁶ induced on the ions after making the small positive and negative displacements (to remove any quadratic effects) about the reference structure positions from total energy DFT calculation. Diagonalization of the dynamical matrix yields the atomic displacement patterns (eigenvectors) and phonon mode frequencies (eigenvalues).

QE Details. In our plane-wave calculations with the QE code, we use norm-conserving⁴⁷ optimized designed nonlocal⁴⁸ pseudopotentials. All atoms are treated using the same valence electron configurations as in VASP, except that in QE, the $5s$ and $3s$ electrons were also included as valence electrons for La and Ni respectively. We sample the BZ using an $8 \times 8 \times 8$ Monkhorst-Pack k -point mesh. A plane-wave energy cutoff of 50 Ry was used for calculation, and found to produce good convergence, as test calculations with higher energy cutoff (up to 75 Ry) yield the same results. We obtain phonon modes and displacement vectors using density functional perturbation theory (DFPT),^{49,50} by constructing the interatomic force constants from the dynamical matrices obtained on a uniform $4 \times 4 \times 4$ q -point grid. The phonon frequencies and vibrational eigenvectors at arbitrary q vectors are then calculated from diagonalization of the dynamical matrix.

We point out here that both implementations of DFT at the LSDA level give structural agreement (Table I). This fact is important for the comparison study we make later which uses various functionals available in the different codes. Each codes yields a small underestimation of the experimental lattice constant which is typical for the LSDA. The QE code more closely reproduces the experimentally measured Ni–O–Ni rotation angles, whereas the VASP code gives a better rhombohedral angle (α_{rho}). For the magnetic structure of LNO, the QE code predicts a spin-polarized ground state in LSDA ($0.45 \mu_B$ local magnetic moment per Ni ion, $0.03 \mu_B$ per O, and a total moment of $1.08 \mu_B$ per 10-atom unit cell), while the VASP package always yields a non-magnetic solution.

For magnetic metals, such as Fe and Cr, the DFT-calculated local magnetic moments are strongly depen-

dent on the atomic volume considered.^{51–53} The spin-polarized/nonpolarized LaNiO_3 discrepancy, which we find between the QE and VASP codes, could therefore originate from the fine details of our pseudopotential methods and their resulting different equilibrium cell volumes. In light of this finding, we take the three different LaNiO_3 configurations from Table I as “model” structures to evaluate the cell volume influence on the calculated magnetic properties.

We report in Table II for the equilibrium atomic volume, spin-exchange energy and local magnetic moment of Ni ion for various LNO structures. We do find a trend that when the LaNiO_3 cell volume is reduced, QE predicts a diminished local magnetic moment and decreased spin-exchange energy. VASP code, however can hardly predict a spin-polarized ground state, even for LaNiO_3 structures with large atomic volume.

Although we have the calculated magnetic discrepancy between the two DFT implementations, we now attempt to resolve which magnetic configuration can most accurately resembles the known experimental situation—an enhanced Pauli paramagnetism. To do so, we further explore the electronic structure of the spin-polarized ground state obtained from the NC pseudopotential calculations of QE. Consistent with the symmetry of the crystal, we find that each Ni-cation carries the same spin moment. Furthermore, the k -space dispersion of the spin-resolved energy bands are almost identical; however, the spin-up and spin-down eigenvalues are rigidly shifted relative to one another. This indicates that the magnetic properties of LNO can be explained in terms of the Stoner model.^{54,55} Here, we compute a Stoner parameter $I = 1.30 \text{ eV}$ from the ratio of the spin-exchange energy split bands (0.59 eV) with the net magnetization ($\Delta m = 0.45$) per Ni cation. The density of states at the Fermi level (E_F), mainly derived from the spin-polarized Ni e_g states, is $n(E_F) = 0.47 \text{ eV}^{-1}$ per spin and this gives a Stoner factor $S = I \times n(E_F) = 0.61$, indicating that spin-polarized LaNiO_3 in QE is far from a ferromagnetic instability ($S \geq 1$). In other words, there should be no stable ferromagnetic (FM) ordering among

TABLE I: Structural parameters obtained for $R\bar{3}c$ LaNiO_3 within the LSDA from the two codes used in this work and their comparison with experimental data (cf. Ref.11.) In the rhombohedral setting, the rotation angle of adjacent NiO_6 octahedra along the trigonal axis is given as $\theta = \arctan(2\sqrt{3}u)$, where $x = u + \frac{3}{4}$.

	Experiment	Theory	
		VASP	QE
x	0.7968	0.787	0.801
a (\AA)	5.3837	5.303	5.322
α_{rho} ($^\circ$)	60.8596	60.72	61.34
$d(\text{Ni-O})$ (\AA)	1.933	1.896	1.922
$\angle \text{Ni-O-Ni}$ ($^\circ$)	164.8	167.9	163.3
θ NiO_6 rotation ($^\circ$)	9.2	7.35	10.0
Ω ($\text{\AA}^3/\text{f.u.}$)	56.2386	53.57	54.89

TABLE II: Equilibrium atomic volumes for different rhombohedral LNO structures given in Table I and their calculated local magnetic moment (in μ_B/Ni) and spin-exchange energy ($\Delta E = E_{\text{LSDA}} - E_{\text{LDA}}$ in meV/unit cell) dependence with respect to the pseudopotential method. Note, the projector augmented wave (PAW) pseudopotential calculations are performed in VASP and those using the norm-conserving (NC) potentials are carried out in QE.

Ω ($\text{\AA}^3/\text{f.u.}$)	PAW		NC	
	μ_{Ni}	ΔE	μ_{Ni}	ΔE
53.57 (VASP)	0.00	0.00	0.28	-4.4
54.89 (QE)	0.08	-0.24	0.45	-16.5
56.24 (Exp.)	0.06	-0.30	0.35	-18.0

the Ni cations. To verify this, we also perform LDA calculations in QE. Comparing the calculated structural and vibrational properties between non-magnetic and spin-polarized

structure is almost same as the spin-polarized case, and the difference between their phonon frequencies are within 15 cm^{-1} . Consistent with what Stoner model predicts, without the stable FM ordering, there is no obvious spin-lattice or spin-phonon coupling within bulk LNO. Based on these findings, we conclude that the spin-polarized LNO predicted by QE is still a reasonable representation of the experimental paramagnetic ground state.²⁴

B. LSDA+ U

A complete description of correlated $3d$ transition metal oxides with narrow valence bandwidths is challenging within a density functional approach due to the limitations of standard exchange-correlation potentials in describing localized electronic states. To remedy this problem, we use “beyond-LSDA” techniques, starting with the LSDA+ U approach. This method is generally regarded to be the most computationally feasible means to reproduce the correct ground states in correlated systems.⁵⁶ In this formalism, the LSDA energy functional is expanded to include an additional on-site orbital-dependent energy term cast as a Hubbard repulsion U and an intratomic Hund’s exchange energy J .

To reduce the ambiguity in the definition of the LSDA+ U parameters, we use the spherically averaged form of the rotationally invariant LSDA plus Hubbard U method⁵⁶ introduced by Dudarev *et al.*,⁵⁷ with only one effective Hubbard term, $U_{\text{eff}} = U - J$. We treat the double-counting term within the fully localized limit.⁵⁸

The change in total energy E_U for including the Hubbard correction to the exchange-correlation potential is

$$E_U(J=0) = \frac{U_{\text{eff}}}{2} \sum_i \sum_{m\sigma} n_{m\sigma}^i (1 - n_{m\sigma}^i), \quad (1)$$

where $n_{m\sigma}^i$ are the spin (σ) and orbital (m) occupation numbers at site i . In the limit where the occupation

matrices are integer and diagonal, the LSDA+ U correction can be understood as a shift in the occupied orbitals ($n_m = 1$) by $-U/2$ to lower energy and by $+U/2$ higher in energy for unoccupied orbitals ($n_m = 0$).

In this study we examine U_{eff} values of 0, 3 and 6 eV for the correlated Ni $3d$ orbitals states; the standard LSDA corresponds to a $U_{\text{eff}} = 0$ eV. We note that throughout the remainder of the manuscript, U denotes the effective Hubbard parameter. We discuss the structural changes induced by varying U in the subsequent sections.

1. Self-consistent Hubbard U

We also calculate a self-consistent U parameter for LaNiO_3 following the scheme developed by Cococcioni and de Gironcoli.⁵⁹ Their approach relies on the fact that the potential U restores the correct piece-wise linear behavior of the system’s total energy as function of electron number, whereas the LSDA functional incorrectly predicts parabolic dependence of energy on occupation number. The effective interaction parameter U is deduced from Janak’s theorem and linear response theory as

$$U = (\chi_0^{-1} - \chi^{-1})_{ii}, \text{ with } \chi_{ij} = \frac{dn^i}{d\alpha_j}. \quad (2)$$

Here n^i is the occupation number of the localized levels at site i and α_j represents the potential shift applied on the localized orbital at site j . The response matrix χ_0 describes the noninteracting contribution to the band structure after application of a potential shift α , while χ represents the fully self-consistent response to the same potential shift. In practice, the first term χ_0 is computed from the first iteration in the self-consistent (SCF) electronic minimization.

We compute the linear response of the occupation number n^i using the LSDA functional and norm-conserving pseudopotentials within the QE package. The full response matrices χ_0 and χ are then computed by performing the linear response calculation within a $2 \times 2 \times 2$ pseudo-cubic supercell (40-atom cell, containing 8 equivalent Ni atoms), which is large enough to give a converged U value and avoid spurious interactions from the local potential α on neighboring Ni sites.

The low-spin Ni $3d$ orbital occupation anisotropy—a fully filled t_{2g} manifold and a quarter-filled e_g shell—suggests that the effective Coulomb repulsion experienced by an electron on different orbitals should also be substantially different.⁶⁰ For this reason, we further decompose the orbital occupancy $n^i \rightarrow n_m^i$ (m is the angular momentum quantum number, and orbital occupation n_m^i here refers to Löwdin atomic charge) into crystal-field split d -manifold contributions by projecting the valence states $|\Psi_{k\nu}^\sigma\rangle$ onto atom-centered sites i with a Löwdin orthogonal atomic basis set $|\phi_m^i\rangle$ as

$$V_U |\Psi_{k\nu}^\sigma\rangle = \frac{U}{2} \sum_i \sum_{m\sigma} (1 - 2n_{m\sigma}^i) |\phi_m^i\rangle \langle \phi_m^i | \Psi_{k\nu}^\sigma \rangle. \quad (3)$$

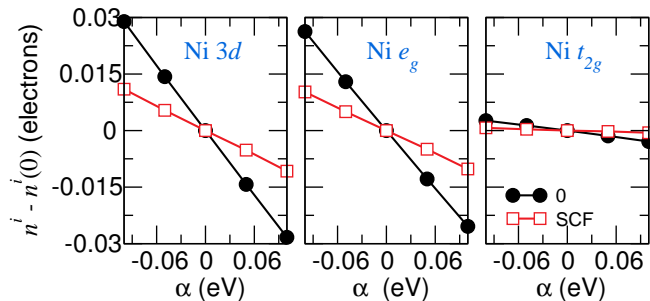


FIG. 3: (Color) The occupation numbers n^i for the total Ni $3d$, e_g and t_{2g} orbitals in LaNiO_3 , with respect to potential shift α for the initial (0) (filled circles) and self-consistent (SCF) (open squares) electronic configurations. The slopes of the linear data fits are used to construct the χ_0 and χ response matrices. The occupation numbers are normalized by subtracting off the occupation values $n_i(0)$ with a zero potential shift ($\alpha = 0$).

By replacing the orbital occupancy n^i in Eq. (2) with n_m^i , we can calculate the effective Hubbard term U for the two independent Ni- d manifolds: $U(e_g)$ and $U(t_{2g})$ respectively. Since the t_{2g} manifold is fully occupied [$n(t_{2g}) \approx 1$], the linear response calculation of $U(t_{2g})$ requires that the contribution from these states to the total Coulomb interaction be nearly zero. Within the numerical noise of our calculations we find this to be the case. Fig. 3 shows that difference in the χ_0 and χ response functions (slopes) of the t_{2g} states is practically negligible. The Ni e_g states, however, which are partially filled have a substantial non-zero interaction, $U(e_g)$. These states lead to a self-consistent Hubbard U value of 5.74 eV for LaNiO_3 .

Recently Nohara *et al.* studied LaNiO_3 with LSDA+ U and GW methods,⁶¹ and fitted their calculated energy spectra to experimental XPS and x-ray adsorption spectroscopy (XAS) data⁶² to obtain a Coulomb interaction of $U = 7.0$ eV and an exchange interaction $J = 1.3$ eV for the Ni d -manifold. These values correspond to an effective Hubbard U term ($U_{\text{eff}} = 5.7$ eV) which is consistent with our linear-response calculation of U .

C. Hybrid Functionals

Recent studies^{31–33,63} have demonstrated that local or gradient-corrected density functionals for exchange do not closely reproduce Hartree-Fock calculations, and that inclusion of some exact Fock (F) exchange improves electronic structure properties including band gaps and orbital localization. Accordingly, in the present work, we use the PBE0 and HSE hybrid functionals as implemented in the QE package and then contrast them to the LSDA.

The exchange terms (V_x) in the PBE0 functional are constructed by mixing 25% of exact-exchange with 75% GGA-PBE exchange,²⁹ while the electron correlation (V_c) part is represented using only the correlation components

from the PBE functional³³:

$$V_{xc}^{\text{PBE0}} = \frac{1}{4}V_x + \frac{3}{4}V_x^{\text{PBE}} + V_c^{\text{PBE}}. \quad (4)$$

The one-quarter mixing parameter of exact exchange in the PBE0 functional was obtained by fitting to the atomization energies of a large database of molecules.²⁹ For periodic bulk systems, however, it is argued that the best fraction of exact exchange for modeling solid-state electronic structure is highly system-dependent.^{29,64}

The HSE hybrid functional^{31,32} is less computationally demanding than PBE0 (unless the recent Wannier function implementation described in Ref.30 is used), since it avoids the slowly decaying Fock-exchange interactions by substituting part of the long-range Coulomb-kernel with a density functional analog. This approximation makes the HSE functional more efficient for plane-wave calculations of periodic systems. The expression for the exchange-correlation potential is given as

$$V_{xc}^{\text{HSE}} = \frac{1}{4}V_x^{\text{sr},\mu} + \frac{3}{4}V_x^{\text{PBE,sr},\mu} + V_x^{\text{PBE,lr},\mu} + V_c^{\text{PBE}}, \quad (5)$$

where μ is the parameter that controls the decomposition of the Coulomb kernel into short-range (sr) and long-range (lr) exchange contributions. This type of screened exact-exchange is absent in the PBE0 functional. In this work, we follow the HSE03 parametrization³¹ which sets the cut-off distance to $\mu = 0.109 \text{ \AA}^{-1}$.

Similar to PBE0, the Fock-mixing parameter in HSE varies approximately in proportion to the inverse static dielectric constant (ϵ_∞^{-1}), and therefore also becomes highly system dependent. For metals with excellent screening, ϵ_∞^{-1} approaches zero. Therefore PBE0 or HSE calculations which incorporate some Fock-exchange may lead to severe overestimation in orbital bandwidths and spin-exchange splitting parameters for such materials.⁶⁵

In our hybrid functional calculations on metallic LaNiO_3 , we use a dense Brillouin zone sampling⁶⁵ for accurate evaluation of the Fock-exchange operator in reciprocal space. We obtain fully converged results on a $8 \times 8 \times 8$ k -point grid for both PBE0 and HSE calculations.

IV. RESULTS AND DISCUSSION

In this section, we present our first-principles results on the structural, vibrational and electronic properties of bulk LaNiO_3 obtained using the various XC-functionals. This section is organized as follows: we first investigate the structural phase transition and temperature-dependent Raman phonon modes of LaNiO_3 using the conventional LSDA approximation. We then examine how the atomic structure, Raman phonon modes and electronic properties of LaNiO_3 are modified with the improved treatment of electron-electron correlation effects. Finally, by comparing the densities-of-states results obtained from the different functionals to the experimental spectroscopic data, we identify which XC-functional best reproduces the intrinsic electronic properties of LaNiO_3 .

A. Structural Phase Transition

The temperature-induced rhombohedral-to-cubic phase transition in LaNiO_3 manifests as a cooperative rotation of nearly rigid NiO_6 octahedra concomitant with a spontaneous lattice strain that shears the crystal along the trigonal axis.⁶⁶ In this section, we show how the structural transition to the rhombohedrally distorted perovskite phase is characterized by a specific soft mode which has a frequency that collapses to zero as the system approaches the cubic phase.³⁷ We note that all results in this section are obtained with the LSDA XC-functional and NC-pseudopotentials as implemented in QE.

1. Minimal Landau Model

In the Landau theory framework for phase transitions, the free energy of the system is expanded in powers of an order parameter that characterizes the transition. From our previous discussion of the low-temperature $R\bar{3}c$ crystal structure of LaNiO_3 , the only free *internal* parameter is the oxygen position x at the 6e Wyckoff site. Therefore, the natural order parameter to characterize the rhombohedral-to-cubic phase transition is a structure-adapted form of the free Wyckoff position: the NiO_6 octahedra rotation angle θ (Fig. 1).

We expand the free energy G in even powers (up to fourth order) of this rotation angle order parameter θ as:

$$G(\theta, T) = G_0(T) + \kappa(T - T_C)\theta^2 + \lambda\theta^4 \quad (6)$$

where κ and λ are temperature-independent coefficients and θ is the angle of rotation about the $[111]$ -direction. We next “freeze-in” the NiO_6 rotation pattern [inset of Fig. 5 (b)] which corresponds to the A_{1g} Raman-mode of the $R\bar{3}c$ phase. In Fig. 4, we show our calculated values of the total energy versus NiO_6 rotation angle θ computed at the LSDA equilibrium volume. Our fit of the data to Eq. 6 yields excellent agreement and approximately corresponds to the free energy at zero temperature $G(\theta, T = 0 \text{ K})$. From the minimum of the free energy $(\partial G / \partial \theta)_T = 0$, we obtain the T dependence of θ :

$$\theta^2 = \frac{\kappa}{2\lambda}(T_C - T), \text{ for } T < T_C, \quad (7)$$

and a critical rotation angle at $T = 0 \text{ K}$ of $\theta_C = 10.04^\circ$ (the optimized θ from the LSDA calculation).

We next calculate the energy stabilization obtained from freezing-in the NiO_6 rotation at 0 K as the difference between cubic and rhombohedral phases, $\Delta E = 172 \text{ meV}/10\text{-atom unit cell}$ given by the well depth from the total energy calculations [Fig. 4(a)]. With increasing temperature, the energy stabilization from the structural distortion decreases until at $T = T_C$, therefore, the thermal excitation energy is equivalent to ΔE and the double-well potential becomes a single well with one minimum at $\theta = 0^\circ$. With these conditions, we write

$$\Delta E = (T \cdot \Delta S)_{T=T_C}, \quad (8)$$

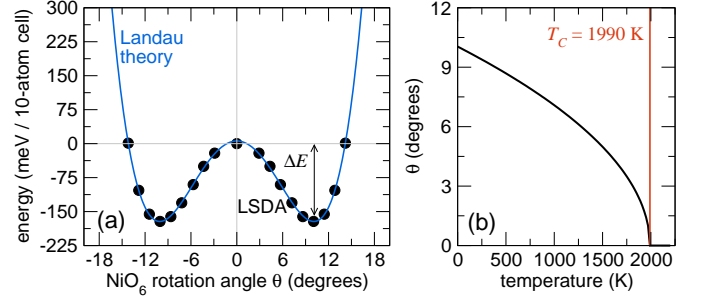


FIG. 4: (Color) (a) Landau free energy $G(\theta, T = 0 \text{ K})$ of LaNiO_3 as a function of the order parameter θ . Solid lines are calculated using Landau theory and the filled symbols correspond to the LSDA total energy results. (b) Equilibrium order parameter θ as a function of temperature; the second order phase transition occurs at $T = T_C$.

where ΔS refers to the entropy difference between the cubic and rhombohedral phases. Since LaNiO_3 has a Debye temperature Θ_D of 420 K,²² at the structural transition $T = T_C$, $T_C \gg \Theta_D$, we are able to confidently treat each lattice mode as an independent harmonic oscillators which subsequently contributes $Nk_B T$ to the free energy.

For the 10-atom rhombohedral LaNiO_3 unit cell, a single soft mode ($N = 1$) describes the transition into the high-temperature cubic phase; therefore, $\Delta S \simeq k_B$. From these conditions, we calculate the LSDA critical temperature for the structural phase transition T_C is 1990 K, which is close to experimental⁶⁶ result ($T_C = 1780 \text{ K}$). The overestimation of T_C likely originates from the calculated enhancement of θ_C , which increases the energy difference between cubic and rhombohedral phases.

Using this calculated T_C value, and combining with our earlier calculated DFT total energy results, we obtain the coefficients in Eq. (6): $\kappa = 1.712 \text{ } \mu\text{eV}/\text{K} \cdot (^\circ)^2$ and $\lambda = 16.9 \text{ } \mu\text{eV}/(^\circ)^4$. These values combined with Eq. 7 give the second-order temperature dependence of the NiO_6 octahedral rotational angle $\theta(T)$ shown in Fig. 4(b).

2. Correlation of volume expansion with phase-transition

With increasing temperature, the LaNiO_3 lattice undergoes a thermal volumetric expansion process. To precisely simulate the temperature induced rhombohedral-to-cubic phase transition process, it is necessary to evaluate the effect of volume expansion on the NiO_6 octahedral rotations across the structural phase transition.

By including the coupling between order parameter θ and the equilibrium atomic volume V , we extend the minimal 1D Landau model discussed in the previous subsection into a 2D case, with the free energy G given as:

$$G(\theta, V, T) = G_0(V, T) + \kappa(V)(T - T_C)\theta^2 + \lambda(V)\theta^4, \quad (9)$$

where V is the equilibrium LaNiO_3 volume at a given temperature, and coefficients κ and λ are expressed as a

function of V . From 0 K to room temperature, we assume a linear volumetric thermal expansion: $V(T) = V_0 \times (1 + \alpha_V T)$, where V_0 is the volume at 0 K and the thermal volumetric expansion coefficient $\alpha_V = 1.624 \times 10^{-5}/\text{K}$ is from experiment.⁶⁶

To correlate the DFT total energy results with the Landau free energy at 0 K, we rewrite Eq. 9 as

$$G(\theta, V, T = 0 \text{ K}) = G_0(V) + A(V)\theta^2 + B(V)\theta^4. \quad (10)$$

This form indicates a practical route to calculate the optimal NiO_6 rotation angle θ_C with respect to V . We apply the procedure described in the previous subsection, but now obtain volume-dependent coefficients A and B by fitting each coefficient through a Taylor expansion about the equilibrium volume:

$$A(V) = A_0 + A_1\left(\frac{\Delta V}{V_0}\right) + A_2\left(\frac{\Delta V}{V_0}\right)^2 + \dots, \quad (11)$$

$$B(V) = B_0 + B_1\left(\frac{\Delta V}{V_0}\right) + B_2\left(\frac{\Delta V}{V_0}\right)^2 + \dots$$

where $\Delta V = V - V_0$. With this method, we obtain the following coefficients: $A_0 = -3.62$, $A_1 = -16.1$, $A_2 = 1.28 \times 10^3 \text{ meV}/(^{\circ})^2$, and $B_0 = 17.1$, $B_1 = -17.5$, $B_2 = -12.3 \times 10^3 \text{ } \mu\text{eV}/(^{\circ})^4$.

This treatment of changes in the lattice volume at the rhombohedral-to-cubic transition reveals that the magnitude of our phenomenological coefficients A (B) increase (decrease) with increasing cell volume. Thus, the curvature of the double-well potential [Fig. 4] becomes steeper and its depth deeper. Our analysis indicates that the thermal expansion effect will hinder the rhombohedral-to-cubic phase transition in LaNiO_3 . Nonetheless, the magnitude of the thermal volumetric expansion is very limited, i.e. from 0 K to room temperature, $\Delta V/V_0 \simeq 0.5\%$, which leads to changes in the coefficients A and B by less than 1% and a deviation in our simulated rotation angle θ at 300 K by 0.2° compared to the volume-independent model previously described. We conclude that, for the temperature range we investigated (0 K to room temperature), treating the phenomenological coefficient in our Landau theory as volume-independent suffices to produce an accurate description of the temperature-induced octahedral phase transition in LaNiO_3 .

3. Temperature-dependent Raman Frequencies

We next study the structural and vibrational properties of LaNiO_3 at finite temperatures. As the temperature increases the NiO_6 rotation angle θ decreases [Fig. 4(b)] and the Ni–O bond length increases. To capture this effect in our simulation, we choose to combine the cell parameters a and α for LaNiO_3 at a given temperature with a specific NiO_6 rotation angle θ and Ni–O bond length $[d(\text{Ni–O})]$. The rotation angle θ for a given temperature is obtained from Eq. 7. While for $d(\text{Ni–O})$, we refer to the experimental temperature-dependent neutron

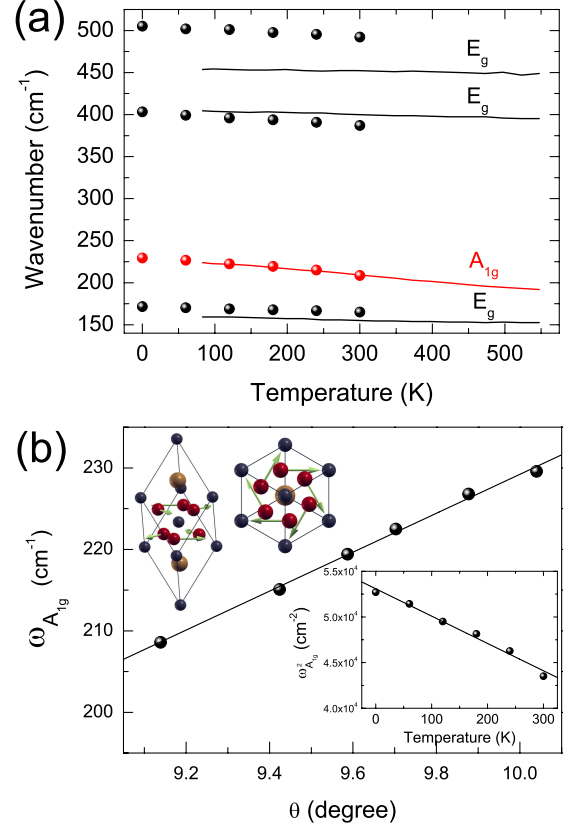


FIG. 5: (Color) (a) Temperature-dependent Raman frequencies for the rhombohedral LaNiO_3 structures. Solid lines indicate experimental results which are taken from Ref.66. Results from our LSDA calculations are given as filled circles. (b) We observe linear scaling behavior between A_{1g} Raman frequency and the NiO_6 octahedral rotation order parameter θ . The solid line is fitted for a guide to the eye. The inset (upper left) shows the vibrational pattern of A_{1g} mode (both side and top view), while the other inset (lower right) shows a linear change in the squared A_{1g} soft-mode frequency with temperature.

scattering results.¹¹ To sample the $d(\text{Ni–O})$ –temperature space at experimental values not available, we assume linear thermal expansion. We then relax only the internal coordinates and use the structures that yield the best experimental agreement to represent a snapshot of the experimental LNO structure.

We use these structures to perform phonon calculations and obtain the temperature-dependent Raman frequencies [Fig. 5(a)]. A comparison of the experimental⁶⁶ data to our DFT calculated temperature-dependent Raman frequencies reveals good agreement: both data sets show red-shifts in the Raman frequencies with increasing temperature. The calculated high-frequency E_g mode, which corresponds to stretching of the Ni–O bonds, however is systematically underestimated by around 10%. The LSDA also predicts that the frequencies of the bending and stretching E_g modes decrease nearly twice as fast as

that experimentally observed.

We now make the connection between the frequency of the A_{1g} Raman mode ($\omega_{A_{1g}}$) present in the rhombohedral structure and how it motivated θ as the order parameter described in the previous subsections. Here, we assign the lattice mode to correspond to the stiffness κ , or the curvature (second-order derivative) of the potential well, as

$$\omega_{A_{1g}}^2 \propto \frac{\partial^2 G}{\partial \theta^2} = 4\kappa(T_C - T), \text{ for } T < T_C. \quad (12)$$

By comparing Eq. 7 with Eq. 12, we find that $\omega_{A_{1g}} \propto |\theta|$ and in the temperature limit $T \rightarrow T_C$ both θ and $\omega_{A_{1g}}$ approach zero. Using our fitted value of κ , we show in Figure 5(b) that $\omega_{A_{1g}}$ varies linearly with θ . We also predict from the slope of Fig. 5(b) that the Raman-mode shift due to changes in the NiO_6 rotation angle is $\omega_{A_{1g}}/\theta = 22.87 \text{ cm}^{-1}/(^{\circ})$. Finally, we plot the temperature-dependence of the squared A_{1g} frequency [Fig. 5(inset)] and find that $\omega_{A_{1g}}^2$ decreases linearly with temperature, confirming the $\omega_{A_{1g}}^2(T)$ relation in Eq. (12). On the basis of these findings, we conclude that the A_{1g} soft mode can be used as a signature for the magnitude of the octahedral rotations in rhombohedral LaNiO_3 and its deviation from cubic phase.

B. Correlation effects on the atomic structure and Raman phonon modes

We focus in this section on how the Raman active mode frequencies are modified through changes in electron-electron correlations. We first decompose the effect of correlation through the Hubbard U term on the structural degrees of freedom by fixing the lattice parameter to that of the experimental $R\bar{3}c$ structure and allowing the internal atomic positions to fully relax. The results of our atomic relaxations for LSDA+ U values of 0, 3, and 6 eV are summarized in Table III. In all cases, the LSDA+ U functional accurately reproduces the known experimental ground state structure with the minor caveats we discuss next.

With increasing correlation, we find that the NiO_6 rotation angle increases beginning from the LSDA structural ground state ($U = 0 \text{ eV}$), which slightly underestimates the rotation angle, to $U = 3 \text{ eV}$ which overestimates it by approximately 1° . With further increase of the Hubbard U value to 6 eV, we find the rotation angle decreases. The consequence of keeping the unit cell volume and rhombohedral angle fixed is that the change in the NiO_6 rotation angle must be accommodated by bond stretching (or compression) rather than through rigid rotations (constant Ni–O bond lengths). Because the Ni atoms also occupy the $2b$ Wyckoff position with $\bar{3}$ site symmetry, all Ni–O bond lengths are required to be equivalent. We thus observe that our calculated Ni–O bond lengths respond proportional to the NiO_6 rotation angle θ (Table III).

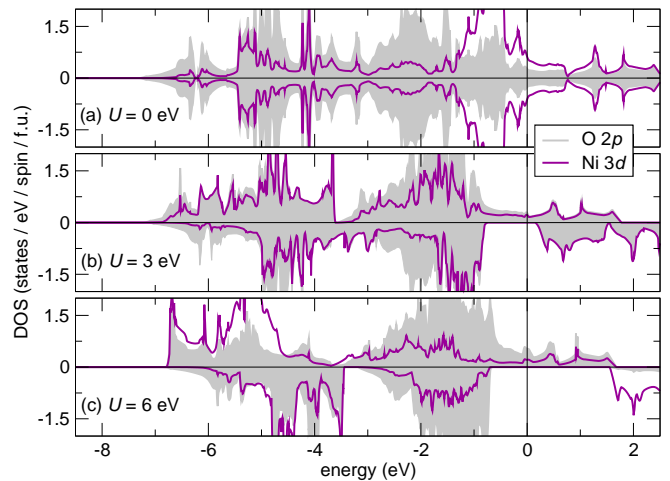


FIG. 6: (Color) Spin- and atom-resolved densities of states (DOS) for the LaNiO_3 structures reported in Table III with the LSDA+ U exchange-correlation functional.

We next examine the change in the electronic structure with increasing correlation to evaluate how the electronic states around the Fermi level are modified. We show in Fig. 6 the electronic densities-of-states (DOS) as a function of the Hubbard U value obtained by LSDA+ U calculations with the VASP code. Consistent with earlier band structures calculations on bulk LaNiO_3 with the LSDA ($U = 0 \text{ eV}$) functional,^{67–69} we find a non-magnetic ground state with localized Ni 3d states peaked centered 1.0 eV below the Fermi level (E_F). A set of delocalized Ni 3d states cross E_F , while the O 2p states are distributed throughout the entire valence band.

Here, we apply a Hubbard U term on the Ni- d states, where we anticipate the on-site Coulomb interaction to localize the itinerant Ni- d electrons at E_F . This leads to a ferromagnetic spin configuration. Indeed, we find a half-metallic ferromagnetic ground state ($1 \mu_B/\text{f.u.}$) with a stable ferromagnetic ordering, which has not been experimentally reported. For $U = 3 \text{ eV}$, we find that the DOS at the Fermi level is substantially suppressed compared to the LSDA, with the Ni d states shifting to lower energy. Due to the increased rotational angle of the NiO_6 , we find a pseudo-gap opens in the majority spin DOS around 3.5 eV with increasing hybridization between the Ni 3d – O 2p states. With further increase of

TABLE III: Optimized internal structural parameters of $R\bar{3}c$ LaNiO_3 at the experimental¹¹ cell parameter a and rhombohedral angle α , calculated with the LSDA+ U functional and PAW pseudopotentials as implemented in VASP.

	Exp.	LSDA+ U (U in eV)		
		0	3	6
x	0.797	0.796	0.800	0.797
$d(\text{Ni-O})$ (\AA)	1.933	1.932	1.935	1.933
$\angle \text{Ni-O-Ni}$ ($^{\circ}$)	164.8	165.2	163.9	164.6
θ NiO_6 rotation ($^{\circ}$)	9.20	8.97	9.77	9.33

TABLE IV: Raman-active vibrational modes computed using the LSDA+ U formalism at the experimental cell volume are compared to the measured values. All mode frequencies are given in wavenumbers (cm^{-1}). The experimental values are taken from Ref.66.

Exp.	E_g	E_g	A_{1g}	E_g	E_g
	—	156	209	399	451
$U = 0$ eV	61.8	155.0	215.4	372.6	451.7
$U = 3$ eV	94.3	164.8	245.5	387.3	413.5
$U = 6$ eV	54.6	156.7	219.4	316.0	381.8

the U value [Fig. 6(c)], we find that most of the majority spin Ni $3d$ electrons are shifted completely to the bottom of the valence band around -5.5 eV. The states at E_F are now mainly O $2p$ character with a small contribution from the Ni $3d$ electrons.

We now compute the Raman active lattice modes for the structures listed in Table III to explore the nonmonotonic trend in the NiO_6 octahedral rotation angle with an increasing Hubbard U value. We begin by comparing the experimentally measured values to our calculated ones (Table IV). The best agreement with the experimental data is for the LSDA ($U = 0$ eV) exchange-correlation functional. A Hubbard U value of 3 eV overestimates the low frequency Raman mode with E_g symmetry (La anti-parallel displacements), while it underestimates the two high frequency E_g modes (Ni-O bond bending and stretching).

Interestingly, with the LSDA+ $U=6$ eV functional we find an unstable (imaginary) zone-center phonon ($246i \text{ cm}^{-1}$) with A_{2g} symmetry indicating that the rhombohedral structure with the simple $a^-a^-a^-$ tilt pattern is unstable. The atomic displacement pattern of the imaginary mode correspond to a three-dimensional checkerboard arrangement of dilated and contracted octahedra—the so called octahedral “breathing” mode that often accompanies charge disproportionation reactions.⁷⁰ This mode, however, has not been observed in any temperature-dependent x-ray studies on LaNiO_3 . We therefore suggest that this correlation-induced octahedral distortion is a spurious artifact of using a large on-site Coulomb repulsion interaction in the the LSDA+ U calculation. We conclude that a Hubbard U value less than 6 eV should be used when simulating LaNiO_3 because of the overall poor accuracy in the calculated Raman modes (Table IV) despite such large Hubbard values closely reproducing the experimental lattice parameters of LaNiO_3 phase (Table III).

We now explore how changes in the electron correlations modify the lattice volume by fully relaxing both the internal atom positions and the rhombohedral structure (Table V). For the LSDA+ U exchange-correlation potential, we qualitatively find the same structural trends as in Table III. While LSDA underestimates the atomic volume, when we increase the value of U , the cell volume increases a little bit; this can be understood as a result from enhanced electrostatic repulsion. We also compute the ground state structures using the PBE and

the PBEsol gradient-corrected exchange correlation functionals to evaluate how the volume changes with these functionals (Table V). For the PBE functional, we find that the cell volume and octahedral rotation angle are overestimated. On the other hand, PBEsol corrects some of this overestimation, although still slightly overestimating the rotation angle, it does provide the best agreement with the experimental lattice constant a , Ni-O bond length and equilibrium atomic volume.

We now use these ground state structures and calculate the Raman-active mode frequencies to examine the effect of lattice volume on the mode frequencies. Comparing these LSDA+ U results (Table VI) to our previously calculated lattice modes obtained using the same functionals but at the experimental volume (Table IV), we find that the LSDA ($U = 0$ eV) functional provides the best agreement with experimental data. As before, we find an unstable zone-centered NiO_6 octahedral breathing mode in our calculations with $U=6$ eV. Interestingly, the LSDA+Hubbard U method accurately predicts the ground state structural properties; however, it also leads to poor predictions for the lattice normal modes. We note that in this case, simply reproducing the correct ground state atomic structure is not a sufficient criteria to evaluate the performance of a functional. This caveat is important to consider especially in the search for perovskite materials with large electron-phonon interactions.

The PBE functional accurately reproduces the frequencies of the two softest Raman modes, while it severely underestimates the two higher energy modes with E_g symmetry. In contrast, the PBEsol functional corrects the frequency underestimation in the E_g modes, but predicts a harder A_{1g} mode, the soft-mode we use as a signature to characterize the structural transition of LaNiO_3 . To summarize, the conventional LSDA functional best reproduces the experimental Raman frequencies.

It is worth noting that the NiO_6 rotation angle θ , the order parameter for the structural phase transition in LaNiO_3 , is highly sensitive to the exchange-correlation functional. Even calculations with same functional, but different pseudopotentials (for example the LSDA calculations performed with the VASP and QE codes) yield θ values with obvious differences. Therefore the accurate and comprehensive study of various theoretical approximations on the descriptions of the octahedra rotation angles in rhombohedral perovskite oxides is needed.

C. Electronic structure and experimental energy spectra

In this section we compare our first-principles results with recent photoemission spectroscopy (PES) data to identify the degree of electronic correlations in rhombohedral LaNiO_3 . In a single electron picture, PES measures the excitation energies for non-interacting electrons from the valence band into the continuum and therefore can be used as a first-order reference to single-particle DFT

TABLE V: Fully optimized structural parameters of $R\bar{3}c$ LaNiO₃ (rhombohedral setting), calculated from the various exchange-correlation functionals.

	Exp.	VASP: LSDA+ U (U in eV)			QE		
		0	3	6	LSDA	GGA-PBE	PBEsol
x	0.7968	0.787	0.795	0.792	0.801	0.815	0.809
a (Å)	5.3837	5.303	5.308	5.319	5.322	5.431	5.354
α_{rho} (°)	60.8596	60.72	60.92	60.83	61.35	61.50	61.40
$d(\text{Ni-O})$ (Å)	1.933	1.896	1.905	1.906	1.922	1.975	1.941
$\angle \text{Ni-O-Ni}$ (°)	164.8	167.9	165.6	165.5	163.3	159.0	160.6
θ NiO ₆ rotation (°)	9.2	7.35	8.76	8.19	10.0	12.7	11.5
Ω (Å ³ /f.u.)	56.2386	53.57	53.97	54.20	54.90	58.53	55.97

studies. We show in Figure 7 experimental PES data²⁷ from a crystalline 20 nm LaNiO₃ film, and compare it with our first-principles calculated valence band DOS to evaluate the accuracy of our calculations in reproducing the known electronic structure. In order to make a more accurate comparison, We first smear our calculated DOS with a Gaussian function (FWHM=0.20 eV) to account for the experimental resolution and multiply by a 20 K Fermi-Dirac distribution, then we convolute an energy-dependent Lorentzian function [full width at half-max (FWHM)= $0.1|E - E_F|$ eV,⁷¹ where E_F is the Fermi level] with our calculated DOS to include lifetime broadening effects of the photon-excited electrons.

The experimental PES consists of four main features: peaks A and B are assigned to the Ni e_g and t_{2g} states, and the deeper C and D spectra to the O $2p$ dominant states.²⁷ The e_g states (A) are clearly resolved as a sharp peak at the Fermi level and the strong t_{2g} peak is located at 1.0 eV below the Fermi edge. The O $2p$ states (c), located below the t_{2g} states, correspond to non-bonding O $2p$ states, as their hybridization with the Ni $3d$ states is restricted by symmetry. While the O $2p$ bonding states (d) are much broader and located between 8 and 3 eV. Compared to experimental PES results, none of the exchange correlation functionals are able to reproduce the sharp spectral intensity of the e_g peak at the Fermi level. Each method leads to an over delocalization of the itinerant e_g electrons (Fig. 7).

Despite the inability to reproduce peak A, the LSDA functional does exceedingly well in reproducing the experimental valence band features—both the correct valence bandwidth and energy peak positions. As shown in Fig.

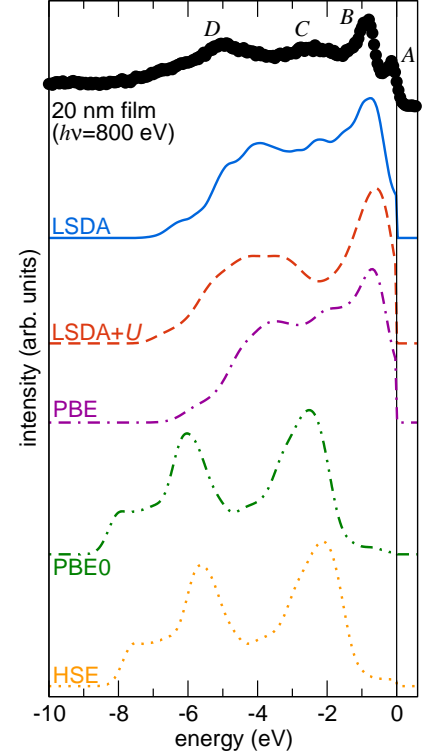


FIG. 7: (Color) The experimental PES spectra for a 20 nm crystalline LNO film (filled circles) (Ref.72) is compared to the density of states calculated with the LSDA+ U ($U=5.74$ eV), gradient-corrected (PBE) and hybrid (PBE0 and HSE) exchange-correlation functionals. The calculated data are smeared with Lorentzian and Gaussian functions and truncated with a Fermi-Dirac distribution to facilitate the comparison. See the main text for peak position assignments.

TABLE VI: Raman-active vibrational modes computed using the various exchange-correlation functionals at the relaxed cell parameters compared to the experimental values.

	E_g	E_g	A_{1g}	E_g	E_g
Exp.	—	156	209	399	451
$U = 0$ eV	72.5	166.4	196.8	374.1	519.4
$U = 3$ eV	73.4	164.0	221.4	388.0	399.4
$U = 6$ eV	66.0	159.6	201.2	330.3	387.3
LSDA-PZ	85.0	171.7	229.6	403.2	505.2
GGA-PBE	92.8	171.5	287.6	355.6	405.8
PBEsol	69.0	168.7	275.7	411.1	469.7

8(a), the LSDA predicts a pronounced hybridization between Ni t_{2g} and O $2p$ states almost throughout the full valence band. The e_g states are predicted to locate at the Fermi level and separated in energy from the Ni t_{2g} orbitals.

The LSDA+ U functional is also able to reproduce the correct bandwidth; however, it fails to predict the correct energy peak positions. Typically, it shifts the t_{2g} states (peak B) toward the bonding O $2p$ states (peak D) as

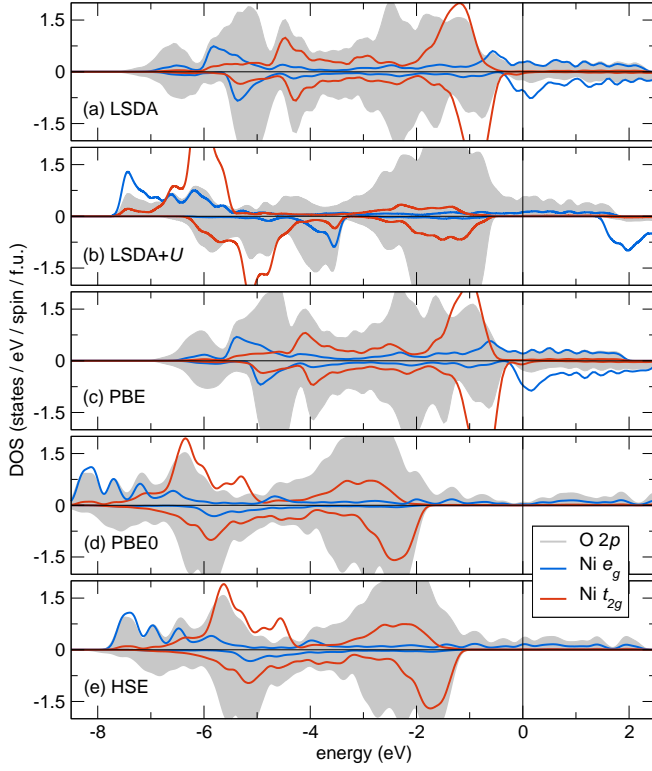


FIG. 8: Spin- and orbital-resolved density of states for rhombohedral LaNiO_3 , obtained from LSDA, LDA+ U ($U = 5.74$ eV), PBE, PBE0 and HSE calculations. The Fermi energy level is shifted to the energy zero. In each case the structure is relaxed according to the specific functional with the exception that the DOS for the hybrid XC-functionals are calculated with the LSDA ground state atomic structure.

observed in the orbital resolved DOS [Fig. 8(b)]. There is an additional shift of bonding O $2p$ spectral weight from the bottom of the valence band to around feature B which gives the impression that the localized t_{2g} states below the Fermi level are only broadened and not shifted. These two effects combine to give a reduced intensity in the non-bonding $2p$ states (peak c), where as experimentally they contribute greater intensity to the PES data. The PBE functional also predicts the correct delocalized electronic characters for LaNiO_3 , but underestimates the valence bandwidth [Fig. 8(c)]. It predicts an electronic structure that is intermediate between the LSDA and LSDA+ U methods.

Both hybrid functionals give poor agreement between the calculated DOS and the experimental PES data. In each case the bandwidth is overestimated, with the PBE0 (HSE) functional ≈ 1.5 eV (1 eV) larger than the experimental results. This is in contrast to the PBE functional which produces a narrow (6 eV wide) valence band [Fig. 8(c)]. As mentioned earlier, similar errors are also found in other itinerant magnetic metals when using the PBE0 and HSE functionals.⁶⁵ The major peaks are also red-shifted by approximately 2 eV, i.e. PBE0 and HSE functionals shift the major Ni t_{2g} states to 7.5-5 eV below E_F . Sim-

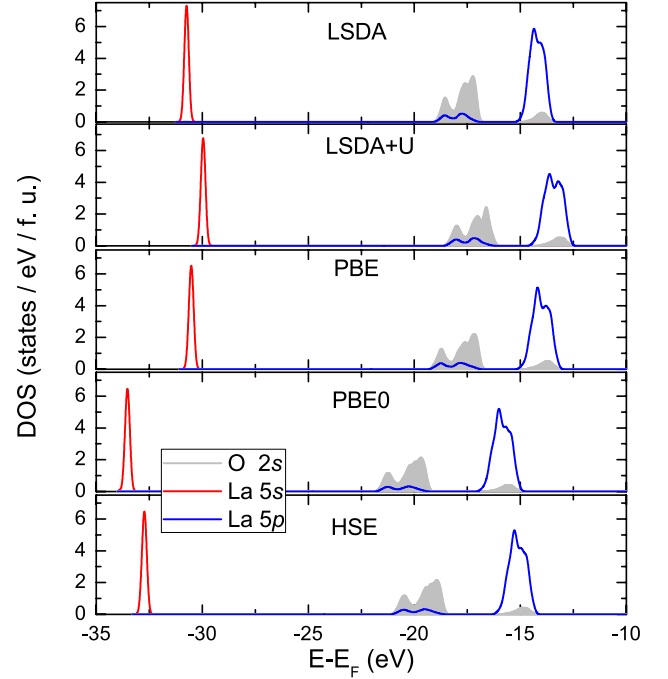


FIG. 9: Orbital-resolved density of states in the core energy region obtained from LSDA, LSDA+ U ($U = 5.74$ eV), PBE, PBE0 and HSE calculations. The Fermi energy level is shifted to the energy zero. It is noted the binding energies predicted by PBE0 and HSE are not simple rigid shift, compared to PBE results.

ilar to the LSDA+ U approach, the hybrid functionals suppress the contribution of Ni states at E_F . This results in the removal of the Ni e_g states from the Fermi level and shifts them to the bottom of the valence band. This shift of electronic states produces the unusual shoulder at -8 eV in the DOS calculated with the hybrid functionals (Fig. 7).

The above comparison to the experimental data clearly indicates that the beyond-LSDA methods (the LSDA+ U and hybrid density functionals) incorrectly describe the electronic structure of LaNiO_3 . The origin for these discrepancies lies in the fact that the valence band is primarily composed of strongly delocalized Ni t_{2g} and O $2p$ states. Therefore, metallic LaNiO_3 is able to strongly screen the electron-electron interactions. This screened electron-electron interaction can lead to renormalization of the electronic states near the Fermi level, which are responsible for the sharp e_g peak observed experimentally.⁷³ The accurate treatment of this phenomenon in LaNiO_3 will require the calculation using many-body DFT methods, i.e. quasi-particle GW , which includes the dynamically screened Coulomb interaction and therefore can treat the electron screening effect in a dynamic (energy-dependent) way.⁷³ Our beyond-LSDA methods, such as LSDA+ U and hybrid functionals,^{61,65} however, only include the exchange-correlation functional, which is independent of the quasi-particle frequency. As such, either the on-site

TABLE VII: Calculated binding energies (in eV) for the major energy peaks in the core region from this study are compared to those calculated with the PBE0 (designated by the *) functional and experimental (Exp.) values, taken from Ref.74. The assignment of the peak positions follows that of Ref.74.

Peak	Exp.	LSDA	PBE	LSDA+ <i>U</i>	HSE	PBE0	PBE0*
b/c	16.7	14.2	14.4	13.6	15.3	16.0	17.1
d	21.0	17.6	17.6	17.0	19.3	19.8	20.7
e	23.6	18.7	18.6	18.0	20.4	21.1	21.8
f	33.5	30.5	30.7	30.0	32.7	33.5	34.8

Coulomb repulsion interaction from LDA+*U*, or exact-exchange energy from hybrid density functionals, are unable to reproduce the screening effects present in LaNiO₃ and this leads to the above-mentioned discrepancies.

The inability of these beyond-LSDA methods to capture the dynamic screening effects also manifests as shifts in core-level binding energies. To explore this effect, we show in Fig. 9 of our calculated orbital-resolved DOS in the core energy region (35 through 10 eV) for LaNiO₃. The discrete core level states are primarily La 5*s*, 5*p* and O 2*s*. They weakly overlap and are easily distinguishable by spectroscopic measurements. In Table VII, we compare our calculated core-level binding energies to recent XPS data.⁷⁴ Although the LSDA method accurately reproduces the delocalized states in the valence region, it largely underestimates the binding energies of the core level states. In contrast, both hybrid XC-functionals significantly improve the description of the peak positions in the core region. Unlike the delocalized valence electrons, the core level states are weakly modulated by the screening effect from the valence region, and therefore exhibit strongly localized electronic characters. In this case, the hybrid functionals, through the addition of Fock-exchange greatly reduce the self-interaction errors present in the LSDA and GGA functionals and therefore substantially improve the calculated energy spectra. We also note that within the LSDA+*U* framework, the Hubbard *U* does not affect the core level states since it is applied only to the valence Ni 3*d* orbitals, and therefore the core level states are only rigidly shifted in energy respect to those calculated with the LSDA functional.

Based on our first-principles calculations, we find that strong hybridization between the Ni 3*d* and O 2*p* states reduce the on-site *d*-orbital Coulomb interaction in LaNiO₃ through enhanced screening. The conventional LSDA method accurately reproduces the valence band structure and also provides the best experimental agreement to the structural properties, while the hybrid exchange-correlation functionals work best for the core level states. We do find one subtle caveat: the Ni *e_g* states experimentally exhibit dynamical correlation effects, which we are unable to capture in either the LSDA, LSDA+*U*, or hybrid functionals. This enhanced spectral weight at the Fermi level has recently been reproduced experimen-

tally through LDA+dynamical mean-field theory (DMFT) calculations,⁷⁵ where a dynamic (frequency-dependent) treatment of the Ni 3*d* electron-electron interactions leads to an enhanced effective mass and optical conductivity.

V. SUMMARY AND CONCLUSIONS

In summary, we have studied the lattice normal modes and electronic properties of the correlated metal LaNiO₃ with first-principles calculations using a variety of exchange-correlation functionals. We examined the rhombohedral-to-cubic structural transition in LaNiO₃ within second-order Landau phase transition theory. We found that the *A*_{1*g*} Raman-active mode acts as a clear descriptor for the magnitude of the octahedral rotations in rhombohedral perovskites. We therefore suggest Raman spectroscopy is a plausible route for quantifying the magnitude of octahedral rotations in perovskite oxides.

Using a linear response method we showed that the correlation effects in LaNiO₃ originate from the Ni-*e_g* orbitals. We then proposed an orbital-dependent effective Hubbard *U* value of 5.74 eV for LaNiO₃ to be used in the LSDA+*U* formalism. By comparing the results obtained from the various functionals with experimental spectroscopic data, we found an accurate treatment of the correlation effects in LaNiO₃ cannot be simply obtained by the LSDA+*U* or hybrid functional methods. We identified that there are strong hybridization effects between the Ni *t*_{2*g*} and O 2*p* within LaNiO₃ that result in enhanced screening capabilities and act to reduce the electronic correlations in the *e_g* orbitals. Among the various DFT exchange-correlation functionals examined, we find that only the LSDA can reproduce both the delocalized valence states while simultaneously providing the best agreement with the experimentally measured lattice dynamics.

Acknowledgments

This work was supported by the U.S. DOE, Office of Basic Energy Sciences, under Contract No. DE-FG02-07ER46431 (GYG) and DE-AC02-06CH11357 (JMR). IG and AMR were supported by the Office of Naval Research under grant no. N00014-09-1-0157. Computational support was provided by a DURIP grant, a Challenge Grant from the HPCMO, and the high-performance computing facilities at the Argonne Center for Nanoscale Materials. This work was also partially supported by the IMI and AQUIFER Programs of the NSF under Award no. DMR-0843934, managed by the International Center for Materials Research, University of California, Santa Barbara, USA. The authors thank S. J. May, J. E. Spanier, and A. Stroppa for useful discussions.

-
- * Electronic address: gaoyang@sas.upenn.edu
† Electronic address: ilya2@sas.upenn.edu
‡ Electronic address: rappe@sas.upenn.edu
§ Electronic address: rondinelli@anl.gov
- ¹ M. Stengel, D. Vanderbilt, and N. A. Spaldin, *Nat. Mater.* **8**, 392 (2009).
 - ² N. Sai, A. M. Kolpak, and A. M. Rappe, *Phys. Rev. B* **72**, 020101 (2005).
 - ³ A. M. Kolpak, N. Sai, and A. M. Rappe, *Phys. Rev. B* **74**, 054112 (2006).
 - ⁴ W. A. Al-Saidi and A. M. Rappe, *Phys. Rev. B* **82**, 155304 (2010).
 - ⁵ G. Herranz, F. Sánchez, B. Martínez, J. Fontcuberta, M. V. García-Cuenca, C. Ferrater, M. Varela, and P. Levy, *Eur. Phys. J. B* **40**, 439 (2004).
 - ⁶ V. Garcia, M. Bibes, L. Bocher, S. Valencia, F. Kronast, A. Crassous, X. Moya, S. Enouz-Vedrenne, A. Gloter, D. Imhoff, et al., *Science* **327**, 1106 (2010).
 - ⁷ S. Mathews, R. Ramesh, T. Venkatesan, and J. Benedetto, *Science* **276**, 238 (1997).
 - ⁸ K.-T. Kim, C.-I. Kim, J.-G. Kim, and G.-H. Kim, *Thin Solid Films* **515**, 8082 (2007).
 - ⁹ M. Jain, B. S. Kang, and Q. X. Jia, *Appl. Phys. Lett.* **89**, 242903 (2006).
 - ¹⁰ P. Murugavel, R. Sharma, A. Raju, and C. Rao, *J. Phys. D: Appl. Phys.* **33**, 906 (2000).
 - ¹¹ J. L. García-Muñoz, J. Rodríguez-Carvajal, P. Lacorre, and J. B. Torrance, *Phys. Rev. B* **46**, 4414 (1992).
 - ¹² M. L. Medarde, *Journal of Physics: Condensed Matter* **9**, 1679 (1997).
 - ¹³ R. Scherwitzl, P. Zubko, C. Lichtensteiger, and J.-M. Triscone, *Appl. Phys. Lett.* **95**, 222114 (2009).
 - ¹⁴ J. Son, P. Moetakef, J. M. LeBeau, D. Ouellette, L. Balents, S. J. Allen, and S. Stemmer, *Applied Physics Letters* **96**, 062114 (2010).
 - ¹⁵ R. Scherwitzl, P. Zubko, G. Lezama, S. Ono, A. F. Morpurgo, G. Catalan, and J.-M. Triscone, *Adv. Mater.* **22**, 5517 (2010).
 - ¹⁶ J. B. Torrance, P. Lacorre, A. I. Nazzal, E. J. Ansaldo, and C. Niedermayer, *Phys. Rev. B* **45**, 8209 (1992).
 - ¹⁷ P. C. Canfield, J. D. Thompson, S.-W. Cheong, and L. W. Rupp, *Phys. Rev. B* **47**, 12357 (1993).
 - ¹⁸ X. Obradors, L. M. Paulius, M. B. Maple, J. B. Torrance, A. I. Nazzal, J. Fontcuberta, and X. Granados, *Phys. Rev. B* **47**, 12353 (1993).
 - ¹⁹ G. Catalan, *Phase Transitions* **81**, 729 (2008).
 - ²⁰ M. Imada, A. Fujimori, and Y. Tokura, *Rev. Mod. Phys.* **70**, 1039 (1998).
 - ²¹ J. B. Goodenough and P. M. Racciah, *J. Appl. Phys.* **36**, 1031 (1965).
 - ²² K. P. Rajeev, G. V. Shivashankar, and A. K. Raychaudhuri, *Solid State Commun.* **79**, 591 (1991).
 - ²³ N. Y. Vasanthacharya, P. Ganguly, J. B. Goodenough, and C. N. R. Rao, *J. Phys. C* **17**, 2745 (1984).
 - ²⁴ K. Sreedhar, J. M. Honig, M. Darwin, M. McElfresh, P. M. Shand, J. Xu, B. C. Crooker, and J. Spalek, *Phys. Rev. B* **46**, 6382 (1992).
 - ²⁵ X. Q. Xu, J. L. Peng, Z. Y. Li, H. L. Ju, and R. L. Greene, *Phys. Rev. B* **48**, 1112 (1993).
 - ²⁶ J.-S. Zhou, J. B. Goodenough, B. Dabrowski, P. W. Klamut, and Z. Bukowski, *Phys. Rev. Lett.* **84**, 526 (2000).
 - ²⁷ K. Horiba, R. Eguchi, M. Taguchi, A. Chainani, A. Kikkawa, Y. Senba, H. Ohashi, and S. Shin, *Phys. Rev. B* **76**, 155104 (2007).
 - ²⁸ J. Tolédano and P. Tolédano, *The Landau Theory of Phase Transitions* (World Scientific, 1987).
 - ²⁹ J. P. Perdew, M. Ernzerhof, and K. Burke, *J. Chem. Phys.* **105**, 9982 (1996).
 - ³⁰ X. Wu, A. Selloni, and R. Car, *Phys. Rev. B* **79**, 085102 (2009).
 - ³¹ J. Heyd, G. E. Scuseria, and M. Ernzerhof, *The Journal of Chemical Physics* **118**, 8207 (2003).
 - ³² J. Heyd, G. E. Scuseria, and M. Ernzerhof, *J. Chem. Phys.* **124**, 219906 (2006).
 - ³³ J. P. Perdew, K. Burke, and M. Ernzerhof, *Phys. Rev. Lett.* **77**, 3865 (1996).
 - ³⁴ V. M. Goldschmidt, *Naturwissenschaften* **14**, 477 (1926).
 - ³⁵ A. M. Glazer, *Acta Crystallographica Section B* **28**, 3384 (1972).
 - ³⁶ H. T. Stokes, E. H. Kisi, D. M. Hatch, and C. J. Howard, *Acta Crystallographica Section B* **58**, 934 (2002).
 - ³⁷ M. V. Abrashev, A. P. Litvinchuk, M. N. Iliev, R. L. Meng, V. N. Popov, V. G. Ivanov, R. A. Chakalov, and C. Thomsen, *Phys. Rev. B* **59**, 4146 (1999).
 - ³⁸ R. J. Angel, J. Zhao, and N. L. Ross, *Phys. Rev. Lett.* **95**, 025503 (2005).
 - ³⁹ P. Giannozzi, S. Baroni, N. Bonini, M. Calandra, R. Car, C. Cavazzoni, D. Ceresoli, G. L. Chiarotti, M. Cococcioni, I. Dabo, et al., *Journal of Physics: Condensed Matter* **21**, 395502 (19pp) (2009), URL <http://stacks.iop.org/0953-8984/21/395502>.
 - ⁴⁰ G. Kresse and J. Furthmüller, *Phys. Rev. B* **54**, 11169 (1996).
 - ⁴¹ G. Kresse and D. Joubert, *Phys. Rev. B* **59**, 1758 (1999).
 - ⁴² J. P. Perdew and A. Zunger, *Phys. Rev. B* **23**, 5048 (1981).
 - ⁴³ D. M. Ceperley and B. J. Alder, *Phys. Rev. Lett.* **45**, 566 (1980).
 - ⁴⁴ P. E. Blöchl, *Phys. Rev. B* **50**, 17953 (1994).
 - ⁴⁵ H. J. Monkhorst and J. D. Pack, *Phys. Rev. B* **13**, 5188 (1976).
 - ⁴⁶ X. Gonze and C. Lee, *Phys. Rev. B* **55**, 10355 (1997).
 - ⁴⁷ A. M. Rappe, K. M. Rabe, E. Kaxiras, and J. D. Joannopoulos, *Phys. Rev. B* **41**, 1227 (1990).
 - ⁴⁸ N. J. Ramer and A. M. Rappe, *Phys. Rev. B* **59**, 12471 (1999).
 - ⁴⁹ S. Baroni, S. de Gironcoli, and A. D. Corso, *Rev. Mod. Phys.* **73**, 515 (2001).
 - ⁵⁰ X. Gonze, *Phys. Rev. A* **52**, 1086 (1995).
 - ⁵¹ H. C. Herper, E. Hoffmann, and P. Entel, *Phys. Rev. B* **60**, 3839 (1999).
 - ⁵² R. Hafner, D. Spišák, R. Lorenz, and J. Hafner, *Phys. Rev. B* **65**, 184432 (2002).
 - ⁵³ R. Soulaïrol, C.-C. Fu, and C. Barreteau, *Journal of Physics: Condensed Matter* **22**, 295502 (2010).
 - ⁵⁴ O. Gunnarsson, *J. Phys. F* **6**, 587 (1976).
 - ⁵⁵ T. Sasaki, A. M. Rappe, and S. G. Louie, *Phys. Rev. B* **52**, 12760 (1995).
 - ⁵⁶ V. I. Anisimov, F. Aryasetiawan, and A. I. Lichtenstein, *Journal of Physics: Condensed Matter* **9**, 767 (1997).
 - ⁵⁷ S. L. Dudarev, G. A. Botton, S. Y. Savrasov, C. J. Humphreys, and A. P. Sutton, *Phys. Rev. B* **57**, 1505 (1998).

- ⁵⁸ M. T. Czyżyk and G. A. Sawatzky, Phys. Rev. B **49**, 14211 (1994).
- ⁵⁹ M. Cococcioni and S. de Gironcoli, Phys. Rev. B **71**, 035105 (2005).
- ⁶⁰ W. E. Pickett, S. C. Erwin, and E. C. Ethridge, Phys. Rev. B **58**, 1201 (1998).
- ⁶¹ Y. Nohara, S. Yamamoto, and T. Fujiwara, Phys. Rev. B **79**, 195110 (2009).
- ⁶² M. Abbate, G. Zampieri, F. Prado, A. Caneiro, J. M. Gonzalez-Calbet, and M. Vallet-Regi, Phys. Rev. B **65**, 155101 (2002).
- ⁶³ X. Wu, E. J. Walter, A. M. Rappe, R. Car, and A. Selloni, Phys. Rev. B **80**, 115201 (2009).
- ⁶⁴ M. Ernzerhof, Chem. Phys. Lett. **263**, 499 (1996).
- ⁶⁵ J. Paier, M. Marsman, K. Hummer, G. Kresse, I. C. Gerber, and J. G. Angyan, J. Chem. Phys. **124**, 154709 (2006).
- ⁶⁶ N. Chaban, M. Weber, S. Pignard, and J. Kreisel, Appl. Phys. Lett. **97**, 031915 (2010).
- ⁶⁷ D. Sarma, N. Shanthi, and P. Mahadevan, Journal of Physics: Condensed Matter **6**, 10467 (1994).
- ⁶⁸ V. I. Anisimov, D. Bukhvalov, and T. M. Rice, Phys. Rev. B **59**, 7901 (1999).
- ⁶⁹ S. J. May, J.-W. Kim, J. M. Rondinelli, E. Karapetrova, N. A. Spaldin, A. Bhattacharya, and P. J. Ryan, Phys. Rev. B **82**, 014110 (2010).
- ⁷⁰ T. Saha-Dasgupta, Z. S. Popović, and S. Satpathy, Phys. Rev. B **72**, 045143 (2005).
- ⁷¹ J. J. Sakurai, *Modern quantum mechanics* (Reading, MA: Addison Wesley, Menlo Park, CA, 1985).
- ⁷² Reused with permission from K. Horiba, Phys. Rev. B, **76** 155104 (2007). Copyright 2007, The American Physical Society.
- ⁷³ R. Eguchi, A. Chainani, M. Taguchi, M. Matsunami, Y. Ishida, K. Horiba, Y. Senba, H. Ohashi, and S. Shin, Phys. Rev. B **79**, 115122 (2009).
- ⁷⁴ Š. Masys, S. Mickevičius, S. Grebinskij, and V. Jonauskas, Phys. Rev. B **82**, 165120 (2010).
- ⁷⁵ M. K. Stewart, C.-H. Yee, J. Liu, M. Kareev, R. K. Smith, B. C. Chapler, M. Varela, P. J. Ryan, K. Haule, J. Chakhalian, et al., Phys. Rev. B **83**, 075125 (2011).